Earth and Planetary Science Letters 357-358 (2012) 366–375

Contents lists available at SciVerse ScienceDirect

Earth and Planetary Science Letters

journal homepage: www.elsevier.com/locate/epsl

Thick crust beneath the Ordos plateau: Implications for instability of the North China craton

Chun-Quan Yu [a,b,*], Wang-Ping Chen [c,1], Jie-Yuan Ning [a,**], Kai Tao [a], Tai-Lin Tseng [d], Xin-Ding Fang [b], Yongshun John Chen [a], Robert D. van der Hilst [b]

[a] Institute of Theoretical and Applied Geophysics, Peking University, Beijing 100871, People's Republic of China
[b] Department of Earth, Atmospheric and Planetary Sciences, MIT, Cambridge, MA 02139, USA
[c] Department of Ocean Science and Engineering, Zhejiang University, Hangzhou 310058, People's Republic of China
[d] Department of Geosciences, National Taiwan University, Taipei 10617, Taiwan, ROC

ARTICLE INFO

Article history:
Received 31 December 2011
Received in revised form
16 September 2012
Accepted 17 September 2012
Editor: P. Shearer
Available online 26 October 2012

Keywords:
North China craton
crustal thickness
Moho
Conrad discontinuity
decratonization

ABSTRACT

Surrounded by seismicity and other manifestations of active deformation, the Ordos plateau, or the western portion of the North China craton (NCC), is a uniquely stable terrane in Asia. Results from virtual deep-seismic sounding and crustal receiver functions suggests that the crust under the eastern Ordos is thicker (at least 60 km) than expected from previous studies and from its modest elevation (~1500 m above sea-level). Receiver functions also reveal a pronounced elastic impedance contrast within the crust (at ~40 km depth), which we interpret as the Conrad discontinuity. The presence of a 20 km thick layer of mafic lower crust between the Conrad and Moho discontinuities would maintain crustal isostasy. The ~1000 km long seismic profile from the Ordos plateau in the west to the North China basin in the east reveals that crustal thickness changes by almost a factor of two across the active Shanxi rift in central NCC (over a distance of only about 100 km). Insofar the current configuration of the lithosphere under the Ordos plateau might serve as a proxy for the initial condition prior to reactivation of the eastern part of NCC—where a cratonic keel no longer seems to exist—our results support the hypothesis that lower crust foundering was due to transformation of a thick mafic lower-crust to a garnet-rich assemblage (possibly caused by hydration associated with subduction during and/or before mid-Mesozoic times).

1. Introduction

Archean shields mark the oldest and the most stable region of continents. The longevity of shields is generally attributed to the existence of a highly viscous, refractory lithospheric mantle "keel", which is neutrally buoyant due a balance between thermal contraction and a depleted chemical composition (e.g., Jordan, 1978, 1981; Pearson, 1999). These deep and, presumably, ancient continental keels are typically characterized by seismic wave speeds that are higher than the global average for those depths (Jordan, 1978, 1988; Polet and Anderson, 1995).

The North China craton (NCC) is overlain by Archean crust (e.g., Liu et al., 1992) but deviates in several ways from the general characteristics of cratons. In terms of both tectonic stability and structure of the lithospheric mantle, there are substantial differences between its western and eastern parts. Along the Shan-Xi graben and farther to the east, the NCC is tectonically active, as manifested by the occurrence of many devastating intra-continental earthquakes (see e.g., Chen and Nabelek, 1988 and references therein; Fig. 1). Moreover, low seismic wave speeds in the shallow mantle inferred from tomography (Zhao et al., 2009; Huang et al., 2009) and thin lithosphere inferred from receiver functions (Chen et al., 2006, 2009) argue against the presence of a thick refractory keel. Indeed, the composition and geochemical characteristics of igneous rocks suggest that the eastern NCC has been reactivated since the Mesozoic, often viewed as a notable example of decratonization (e.g., Gao et al., 2008; Griffin et al., 1998; Menzies et al., 1993, 2007; Wu et al., 2005).

In contrast, the western part of the NCC, or the Ordos plateau, has been tectonically stable since the early Proterozoic (Kusky et al., 2007; Zhao et al., 2005) and seems to be underlain by a thick keel of high seismic wave speeds (Chen et al., 2009; Huang et al., 2009; Li and Van der Hilst, 2010). The plateau is surrounded by active tectonic belts delineated by abundant historical

* Corresponding author. Department of Earth, Atmospheric and Planetary Sciences, MIT, Cambridge MA 02139, USA. Tel.: +1 6177554858.
** Corresponding author. Tel.: +86 13261838341.
E-mail addresses: yucq@mit.edu (C.-Q. Yu), njy@pku.edu.cn (J.-Y. Ning).
[1] Formerly at Department of Geology, University of Illinois, Urbana IL 61801, USA.

0012-821X/$ - see front matter © 2012 Elsevier B.V. All rights reserved.
http://dx.doi.org/10.1016/j.epsl.2012.09.027

seismicity (562 Brigade, 1979; Fig. 1) and its stability is corroborated by a thick cover of undeformed sedimentary rocks, reaching thicknesses of up to 10 km in places and dating back to the middle Proterozoic (Yuan et al., 2007).

Whereas remobilization of the eastern NCC has been the topic of much debate, little attention is paid to deep crustal properties of the western NCC (cf. Gao et al., 2004; Menzies et al., 2007; Xu, 2001). Judging from its modest elevation of about 1500 m, Airy isostasy predicts a crustal thickness of about 45–50 km beneath the Ordos plateau, a value that has been generally accepted by previous studies of crustal structure in this area (e.g., Li et al., 2006; Tian et al., 2011; Zheng et al., 2012). If correct, this inference from the Airy model would imply that there are only modest variations in crustal thickness between the eastern and western NCC.

With new seismic array data and an innovative method to construct deep seismic profiles over a distance of about 1000 km across the NCC, we show that across the Shan-Xi graben—over a lateral distance of ~100 km—crustal thickness increases westward by more than 20 km to over 60 km beneath the eastern margin of the Ordos plateau. Our results also reveal a strong interface near 40 km depth beneath the Ordos plateau. In previous studies of crustal structures at other locations of the Ordos plateau, this interface was identified as the Moho (e.g., Teng et al., 2010; Tian et al., 2011; Zheng et al., 2012). However, clear evidence for a deeper, strong interface around 60 km, and modeling of scattered *P*- and *S*-waveforms indicates that the interface near a depth of 40 km is likely the Conrad discontinuity between the upper crust and a compositionally distinct lower crust. The lower crust, likely of mafic composition (mafic granulite not yet transformed to eclogite), maintains crustal isostasy and provides a constraint on the initial condition of the NCC before remobilization.

2. Data and methods

We analyze broadband waveforms collected by Peking University between 2007 and 2010 as part of the Destruction of the North China Craton Project. Overall, six linear segments are combined to form an approximately east–west trending profile over a distance of about 1000 km (Fig. 1a). The deployment of each segment, at a station spacing of 10–15 km, lasted about 1 yr.

We use two complementary methods to investigate the crust and the upper mantle under the area of study: virtual deep seismic sounding (VDSS) developed by Tseng et al. (2009) and traditional receiver functions (RFs; Langston, 1979; Ammon, 1991). VDSS produces large, clear reflections that are insensitive to details of the Moho, thus providing a robust estimate of overall crustal thickness. In contrast, signals of interest in RFs are often small in amplitude but are more sensitive to impedance contrasts across subsurface discontinuities than VDSS. In their simplest forms, both approaches assume laterally homogeneous structures; thus we also augment these investigations with finite-difference modeling of laterally varying media.

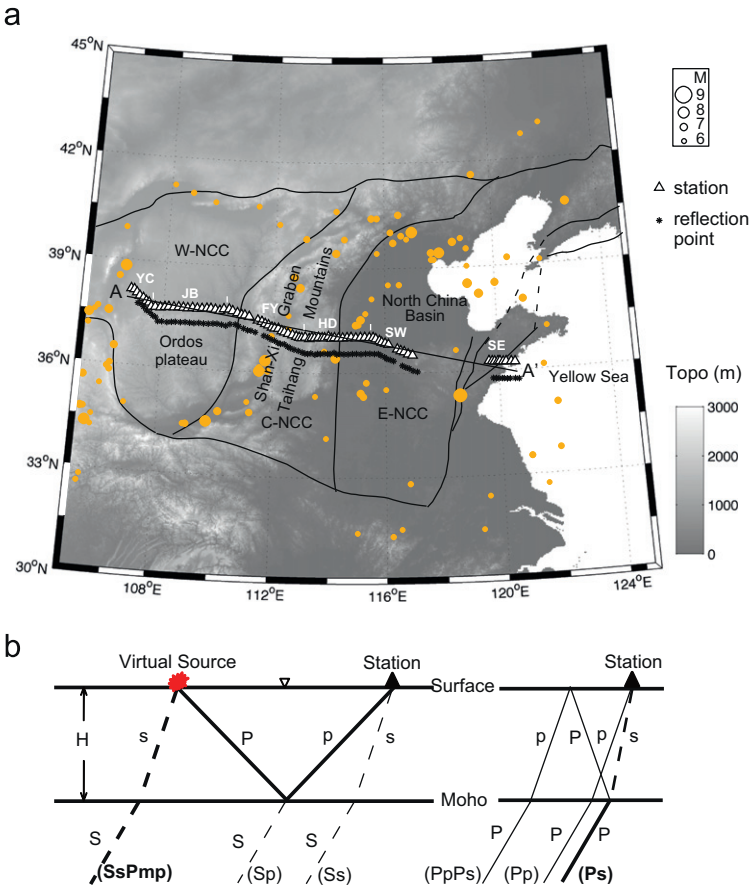

Fig. 1. (a) Topographic map (in gray-scale) showing locations of seismograph stations (open triangles) and corresponding positions of reflection off the Moho for the *SsPmp* phase (asterisks; estimated using a nominal crustal thickness of 40 km). Two-letter codes refer to individual segments of the long seismic profile. Solid curves are boundaries of distinct geologic units within the North China craton (NCC; W-, C- and E- mark the western, central and eastern NCC, respectively; after Zhao et al. 2005). Circles (in bronze) depict epicenters of large historical earthquakes ($M \geq 6$) between 1 and 2010 CE. (b) Schematic cross-sections illustrating paths of main seismic phases related to scattering of teleseismic (left) *S*-wave and (right) *P*-wave near the receiver. (For interpretation of the references to color in this figure caption, the reader is referred to the web version of this article.)

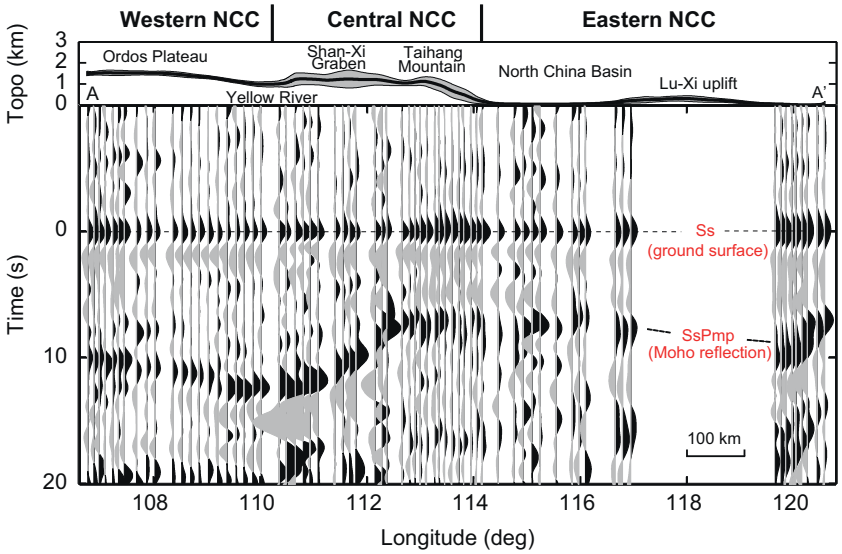

Fig. 2. An east–west trending seismic profile over a distance of more than 1000 km across the NCC. The upper panel shows the mean elevation along the profile, with gray shading indicating variations in topography (at one standard deviation) between each station and its corresponding virtual seismic source. The lower panel shows unprocessed (except for band-pass filtering between 0.02 and 0.5 Hz) seismograms (vertical component of ground velocity). The seismograms are aligned on the direct *S*-wave arrival (*Ss* phase), and the *SsPmp* phase is the wide-angle reflection off the top of the Moho. To a first approximation, the differential travel-time between the two phases ($T_{SsPmp\text{-}Ss}$) is proportional to crustal thickness. Notice large amplitude of the *SsPmp* phase, highlighting pronounced variations in crustal thickness across the NCC.

Unlike conventional seismic profiling with manmade sources near the surface, VDSS utilizes the conversion of teleseismic *S*- to *P*-waves at the free surface (near the receiver) as a virtual seismic source (Fig. 1b). The crustal thickness (H) is then inferred from the differential time between *SsPmp* and *Ss* arrivals:

$$T_{SsPmp-Ss} = 2H(1/V_P{}^2 - p_\beta{}^2)^{1/2} \quad (1)$$

where p_β is the ray-parameter (horizontal slowness) of the incoming *S*-wave, and V_P is the average *P*-wave speed in the crust.

Among numerous earthquakes that occurred during each phase of the deployment, we choose large to moderate-sized events between distances of 30° and 50° for which the amplitude of the relevant seismic phases is expected to be large. Furthermore, we concentrated on deep- and intermediate-focus earthquake to achieve good signal-to-noise ratios (as direct body-wave arrivals go through the highly attenuative upper mantle only once) and to avoid interference from strong reflections near the source. For these events, the amplitude of the *SsPmp* phase is sufficiently large to produce a seismic section from a single event. This approach removes the need for stacking, therefore bypassing the unstable process of deconvolution which would have been required to normalize source wavelets from different earthquakes. We then combine all segments of the deployment using results whose angles of incidence (or ray-parameters) of the incoming *S*-waves are nearly constant across the entire array. For detailed description of the methodology, see Supplementary material S1 and Tseng et al. (2009).

Conventional RF exploits *P*-to-*S* conversions produced by the direct *P*-wave from teleseismic sources (Fig. 1b). The standard approach is to deconvolve the radial component of the *P*-wave trace in the frequency domain, using the corresponding vertical component as the reference signal. Effectively, this procedure removes the source time-function and the effects of wave propagation far from the receiver. RFs that share a narrow range of back-azimuths and ray parameters are then linearly stacked (after corrections for move-outs) to enhance coherent *P*-to-*S* conversions (Supplementary material S1). The differential time $T_{Ps\text{-}Pp}$ between the direct *P*-arrival (*Pp*) and the primary conversion across the Moho (*Ps*) is

$$T_{Ps-Pp} = H\sqrt{(K/V_P)^2 - p_\alpha{}^2} - H\sqrt{1/V_P{}^2 - p_\alpha{}^2} \quad (2)$$

where p_α is the ray-parameter of the incident *P*-wave and $K = V_P/V_S$, the ratio between average *P*- and *S*-wave speeds in the crust (a value directly related to the Poisson's ratio).

In addition to seismic profiles constructed directly from VDSS and RF, we migrate receiver function profiles and carry out waveform modeling at selected stations to investigate specific structural features that are important for geological interpretations.

3. Results

3.1. Crustal thickness from VDSS

Fig. 2 shows the result of VDSS in a composite profile using the vertical-component of ground velocity from three deep- and intermediate-focus earthquakes beneath the Banda Sea, with a back-azimuth of 150–165° (Table 1). The most salient features of the VDSS are shared by both the vertical and the radial components of the data. In the following analysis we will focus on the vertical component, but we also show corresponding profiles from the radial component in Supplementary material (Fig. S1b).

Taking advantage of the large amplitude of the *SsPmp* phase (whose identification is confirmed through waveform modeling—see Section 3.3), we obtained this seismic profile of high signal-to-noise ratios with little processing of the data: we simply applied a zero-phase, band-pass filter (between 0.02 and 0.5 Hz) and then aligned and normalized the amplitudes of the direct *S*-wave arrival (the *Ss* phase in Fig. 1b). The strong *SsPmp* arrival allows easy correlation among adjacent stations to identify the overall configuration of the Moho.

The most important finding is that the differential arrival-times between *SsPmp* and *Ss* are large ($T_{SsPmp\text{-}Ss}$ up to ~12 s) for stations on the Ordos plateau (Fig. 2), indicating a thick crust. For nominal value of average V_P (6.3 km/s), the differential times indicate that crustal thickness reaches a maximum of over 60 km beneath the eastern margin of the plateau. Then over a lateral distance of only 100 km, the crust thins eastward to only ~35 km in thickness ($T_{SsPmp\text{-}Ss}$ ~7 s) under the Shan-Xi graben. This result is robust and reproducible from a number of other earthquake sources (Fig. S2). Farther to the east, $T_{SsPmp\text{-}Ss}$ is also about 7 s, indicative of ordinary

Table 1
Earthquake sources for constructing VDSS profile in Fig. 2.

Segment	Event No.	Date	Origin time[a] (UT)	Lat. (°N)	Lon. (°E)	Depth (km)	Magnitude (M_W)	Back-azimuth (deg.)	Distance (deg.)	Ray-parameter (*Ss* phase) (s/km)
YC	1	2008-04-29	19:10:02	−6.11	127.48	404	5.9	151.7–152.5	47.6–48.3	0.1246–0.1253
JB	1	2008-04-29	19:10:02	−6.11	127.48	404	5.9	152.7–155.7	46.7–47.5	0.1254–0.1261
FY	2	2007-06-06	11:28:24	−6.72	130.91	86	5.8	152.1–155.0	46.8–48.4	0.1266–0.1281
HD	1	2008-04-29	19:10:02	−6.11	127.48	404	5.9	159.4–162.9	44.5–45.2	0.1275–0.1281
SW	3	2009-12-26	08:57:27	−5.53	131.21	83	6.1	157.7–159.3	44.1–44.9	0.1299–0.1306
SE	3	2009-12-26	08:57:27	−5.53	131.21	83	6.1	163.0–164.3	42.9–43.2	0.1314–0.1316

[a] Hypocenter information from USGS NEIC earthquake catalogue.

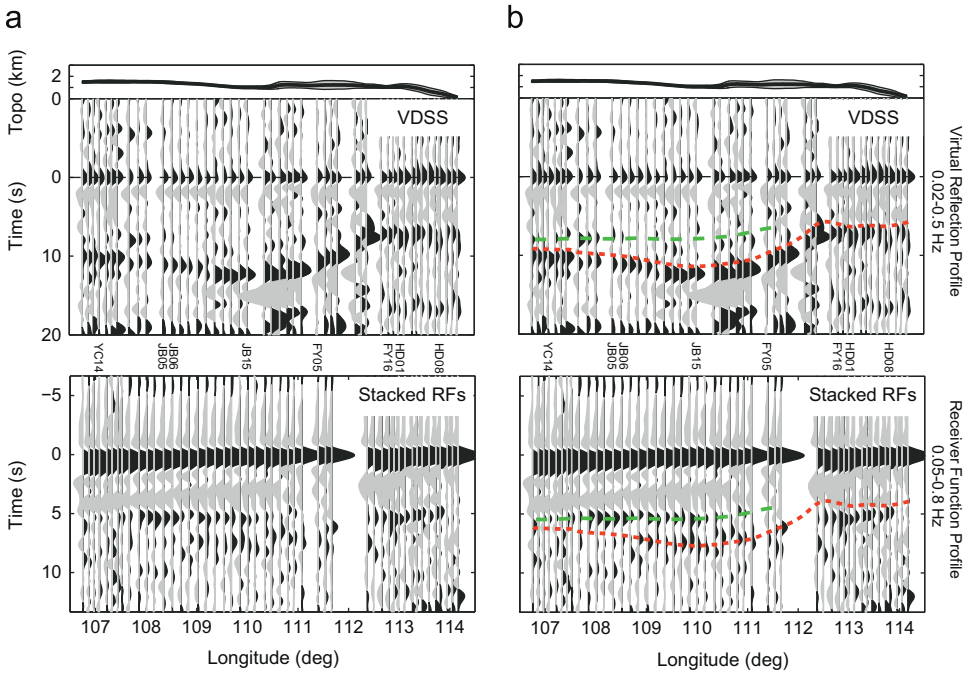

Fig. 3. Comparison between seismic profiles from virtual DSS (top panels) and from conventional receiver functions (stacked but un-migrated; lower panels) across the Central and Western NCC. (a) and (b) show the same two profiles before and after visual interpretations of major discontinuities, respectively. The layout is the same as that of Fig. 2. For direct comparison between the top and the lower panels, the vertical axes of the latter are stretched by a factor of 1.5. Red curves mark manually picked arrival-times of the *SsPmp* phase based on visual inspection of the data in the upper-left panel. Using data only in the lower-left panel, green curves indicate manually picked arrivals of a clear *P*-to-*S* conversion. Earthquake sources used for the stacked RF profile have back-azimuths between 144° and 169°. (For interpretation of the references to color in this figure caption, the reader is referred to the web version of this article.)

continental crust. There is little lateral variation in crustal thickness until one reaches the easternmost end of the profile where the crust thins toward the passive margin of the Yellow Sea (Fig. 2).

3.2. Comparison between RF and VDSS

Hereinafter we focus on the western part of the profile (west of about the 114°E meridian) where the most pronounced changes in crustal properties occur and the station density is highest. In the bottom panel of Fig. 3a, we show a profile of stacked RFs. Earthquakes used to construct this profile are from a source area at about the same back-azimuth as those used for the VDSS (Fig. 2), facilitating a direct comparison between VDSS and RF. It is worth noting that stacked RFs constructed from earthquakes at different back-azimuths show similar results (Fig. S3). The lack of azimuthal dependency in RF indicates that effect from structural variations normal to the trend of the array is minimal. Assuming nominal values of average V_P (6.3 km/s) and Poisson's ratio (0.25) in the crust (e.g., Christensen and Mooney, 1995), we stretch the time-axis of RFs by a factor of about 1.5 so that the primary features surrounding the lower crust are approximately aligned in both types of profile.

At first glance, the strongest signals from the subsurface in the two types of profile do not coincide (Fig. 3a). RFs reveal a conspicuous pulse near $T_{Ps\text{-}Pp}\sim 5$ s under most of the Ordos plateau. The positive polarity indicates that elastic impedance increases with depth. Earlier RF studies at other locations of the Ordos plateau (e.g., Tian et al., 2011; Zheng et al., 2012) interpreted the *P*-to-*S* conversions near 5 s as the *Pms* phase, yielding a crustal thickness of about 40 km, only slightly more than that beneath the eastern NCC. However, the late *SsPmp* arrivals (from VDSS) require a prominent interface at much greater depths.

Closer inspection shows that the RF and VDSS results are consistent. The deeper interface is also visible in the RFs at a number of stations (between 108° and 111°E, Fig. 3b), while the shallower interface also shows up on some of the VDSS traces (Fig. 3b). As such, the most straightforward interpretation is that there are two interfaces at depth, each emphasized either by *SsPmp* or by *Ps* – a result corroborated by waveform modeling (Section 3.3). The sub-horizontal interface from RFs is weak to absent between about 110.5° and 112.5°E (Fig. 3a). Farther eastward beneath the Taihang Mountains, only a single interface at a modest depth is detected.

Visually, a negative pulse precedes the *Ps* phase in many RFs. Although it may be tempting to attribute the negative pulses as

an indication of a crustal low velocity zone, the most straightforward interpretation is that this part of the signal is associated with multiples from a thick sedimentary cover, as confirmed by results of modeling (see Supplementary material S3 for more detail analysis; Fig. S5). This conclusion is consistent with crustal structures obtained from the traditional DSS technique (Jia and Zhang, 2005).

3.3. Waveform modeling using 1-D approximations

For a quantitative investigation of the two interfaces identified above, we compare observed seismograms and their synthetic counterparts produced with the reflectivity algorithm for layered media (Randall, 1989). We focus on the most salient features in the waveforms, including seismic phases *Sp*, *Ss* and *SsPmp* associated with the *S*-wave and *Pp* and *Ps* with the *P*-wave. Additionally, when the signal is clear, we use the phase *PpPs* (a crustal reverberation) along with *Ps* to estimate the average Poisson's ratio of the crust (Supplementary material S2; Fig. S4). Gradual transitions in seismic properties are approximated by a stack of thin layers, each with a thickness of about 6 km. At a dominant frequency of 0.5 Hz, this value is approximately half the wavelength of *P*-waves in the crust. When required by the data, our models also include thick sediments near the surface (mostly represented by a single layer). In most cases, a simple model of about three layers is sufficient to represent the crust (Figs. 4a–c, 5,

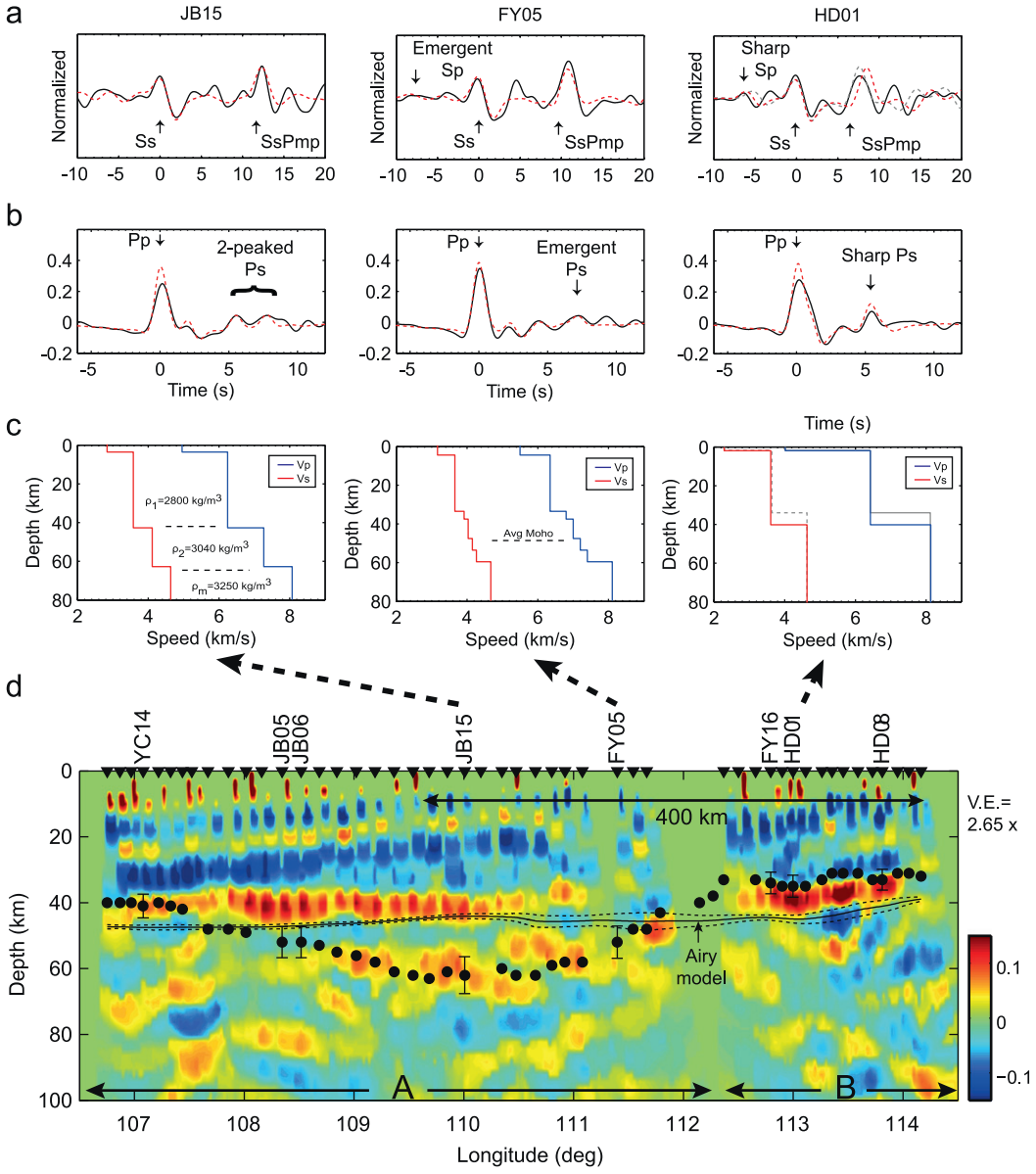

Fig. 4. Quantitative analyses of both *S*-to-*P* and *P*-to-*S* conversions and resulting crustal models at representative stations over the Central and Western NCC. (a) Waveform modeling of the S-wave record. Solid and dashed curves are observed and synthetic seismograms, respectively. (b) Waveform modeling of conventional, *P*-to-*S* receiver functions. The layout is the same as in (a). (c) Resulting crustal models from analyses shown in (a) and (b). For station HD01, phases *Ps* and *SsPmp* result in slightly different best-fitting models (shown in red and gray, respectively). (d) Cross-sectional image of the lithosphere beneath western and central NCC from 2-D, Kirchhoff migration of stacked receiver functions. Results are normalized according to the *Pp* amplitude at each station. Regions A and B are migrated with two different, laterally average crustal models from 1-D waveform modeling. For comparison, position of the Moho obtained from modeling of *S*-to-*P* conversions is marked by solid dots directly beneath their corresponding stations. Note that each Moho reflection point is slightly farther to the east of its corresponding station by about 0.25° for a 40-km thick crust. This value is about 0.5° if the crust is 60-km in thickness. Representative estimates of uncertainties (one standard deviation; assuming average variation of $\pm 3\%$ in V_P) are shown as error-bars at selected stations. The solid curve shows predicted values of crustal thickness from Airy isostasy (dashed curves mark one standard deviation from the mean elevation). (For interpretation of the references to color in this figure caption, the reader is referred to the web version of this article.)

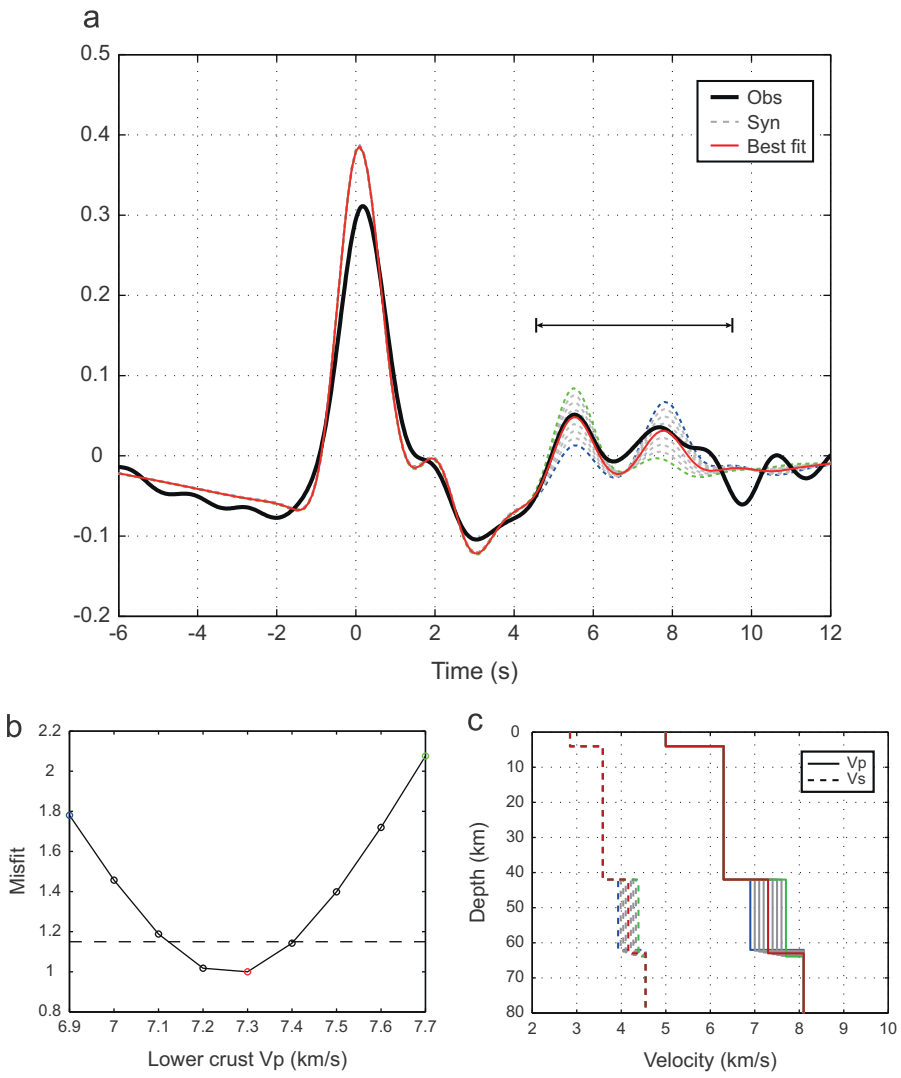

Fig. 5. Determination of uncertainties in crustal models. (a) Comparison of observed and synthetic receiver functions for station JB15. Color codes refer to different cases shown in (c). (b) Variation of misfit between observed and synthetic waveforms for different values of V_P in the lower crust. In defining the misfit, we used the L2-norm of the difference between observed and synthetic seismograms within the time-window of 4.5–9.5 s (double-headed arrows in (a)). The misfit corresponding to each trial model is then normalized by the L2-norm of the difference between observed and best-fitting synthetic seismograms. The dashed line marks the threshold ($\sim$15% increase in misfit from the best-fitting value) above which corresponding models are rejected. Notice that this cut-off is near where the curvature of the curve changes significantly. (c) A suite of crustal models investigated. (For interpretation of the references to color in this figure caption, the reader is referred to the web version of this article.)

and S7). Although more complicated models that have additional degrees of freedom, such as an additional layer for the sediments (Fig. S5), can improve the fitting between data and synthetic seismograms, such features are of secondary importance in investigating the two key interfaces shown in Fig. 3.

For most stations across the Taihang Mountains (east of the 112.5°E meridian, region B in Fig. 4d) the phases *SsPmp* (in VDSS) and *Ps* (in RFs) appear as simple, distinct pulses (e.g., station HD01, Fig. 4a and b). These waveforms can be modeled with a simple, two-layered crustal model. The crustal thickness estimated from VDSS appears to be slightly thinner (by $\sim$5 km) than that from RFs. However, considering that the crust thins toward the east beneath the North China basin (Fig. S3; Jia and Zhang, 2005), and that the *SsPmp* phase samples a much wider swath of the crust along the back-azimuth (southeast) than the *Ps* phase, such a difference is probably of little geological significance.

Clear *SsPmp* arrivals indicate that the crust thickens rapidly westward, reaching a maximum of over 60 km beneath the eastern portion of the Ordos plateau (Figs. 2–4). For example, at station JB15, a large value of $T_{SsPmp\text{-}Ss}$ ($\sim$11.7 s) corresponds to a total crustal thickness of about 63 km. Direct evidence for a mid-crustal discontinuity under this station comes from the *Ps* phase: instead of a single, narrow pulse, this phase is broadened into two separate peaks (Fig. 4b). This feature is consistently observed at other stations over a distance of about 300 km (Fig. S7). In the *S*-wave data, small, double-peaked *Sp* phase predicted by our preferred model has about the same amplitude as the noise. In contrast, the amplitude of *SsPmp*, a post-critical reflection, is not diminished, even though the impedance contrast across the Moho may be reduced by the existence of a distinct lower crust (Fig. 4a and c). Meanwhile, pre-critical reflection off the top of the lower crust is barely discernible between phases *Ss* and *SsPmp* (Fig. 4a).

We also investigated the allowable range of V_P and V_S in the lower crust. Under the constraint that $T_{SsPmp\text{-}Ss}$ and $T_{Ps\text{-}Pp}$ vary within $\pm$0.2 s of observed values, we conduct a systematic search of three model parameters: V_P and V_S of the lower crust, and the total crustal thickness. The observed amplitudes of the double-peaked *Ps* phase at JB15 requires that V_P in the lower crust does not deviate by more than 0.2 km/s from the best fitting value of 7.3 km/s (Fig. 5), a typical value for lower continental crust of mafic composition (Christensen and Mooney, 1995). The estimated uncertainties will increase slightly, by about 0.05 km/s, if

we also allow *Vp* of the upper crust or the uppermost mantle to vary by ± 0.1 km/s. Overall, the best fitting values of V_P for the lower crustal are 7.2–7.6 km/s for stations between 108° and 111°E (Fig. 3b). Note that V_S (and thus the Poisson's ratio) in the lower crust is not well constrained due to the lack of Moho-related multiples on RFs.

3.4. Migration of the receiver function profile

The spacing of RFs is dense enough for a formal migration (Fig. 4d). We used the 2-D Kirchhoff method of Wilson and Aster (2005). This algorithm is designed for configurations where the source is in the same plane as the profile, so we adjusted it slightly to accommodate the source-receiver geometry considered here. This adjustment is justified under the observation that there is little variation in lithospheric structure normal to the profile (see Section 3.2). We note that the image shown in Fig. 4d is for a sub-vertical plane, dipping about 74° toward the south. We account for this effect by projecting the results at each depth horizontally onto an east–west trending vertical plane beneath the receivers. These simplifications are justified because for most stations a simple, 1-D approximation is sufficient to explain waveforms of both *Ps* and *SsPmp* phases (Figs. 4 and S7), whose Moho conversion/reflection points are approximately 11 and 52 km south of the receiver, respectively (assuming 40 km of nominal crustal thickness).

To account for lateral (east–west) variations in crustal properties along the cross-section we splice two average crustal models in the migration (regions A and B; Fig. 4d). Each model represents lateral-averaged crustal properties obtained from waveform modeling of selected stations marked in the very top of Fig. 4d. The main differences between the two models are the inclusion of a lower crust (with a thickness of ~20 km) for region A.

As expected from Fig. 3, the mid-crustal discontinuity stands out over a distance of about 300 km between 108°E and 111°E (Fig. 4d). When the *Ps* phase from the Moho is distinct, so is the image of the Moho after migration (Fig. 4d), resulting in better lateral continuity of the Moho than the un-migrated profile (Fig. 3). For VDSS, at each station we first determined $T_{SsPmp\text{-}Ss}$ precisely by comparing observed and synthetic seismograms. Using the same average crustal models as for RF migration we then calculated crustal thickness from $T_{SsPmp\text{-}Ss}$ (shown as solid dots in Fig. 4d). Overall, the *SsPmp* and *Ps* phases give consistent results in total crustal thickness.

Uncertainties in crustal thickness come from three main sources: errors in differential travel-times, variations in average crustal V_P, and deviations from 1-D approximation. Errors in observed timing have a minor effect: a typical error of ± 0.2 s in $T_{SsPmp\text{-}Ss}$ leads to an error in crustal thickness (H) of only ± 1 km. Variations in average crustal V_P potentially have a larger effect. For $H=30$ km, a fluctuation in V_P of 0.2 km/s (about 3%) causes an error of 2.5 km in H. This error is proportionally larger for a thicker crust (Fig. 4d and Eq. (1). A third source of uncertainty is in the 1-D approximation on which VDSS and RF are based. This effect will be investigated in the next section.

3.5. Waveform modeling: further analysis

Lateral variations in crustal properties depicted in Fig. 4 raise the question of whether waveform analysis based on 1-D models is adequate. Qualitatively, effects of deviation from layered

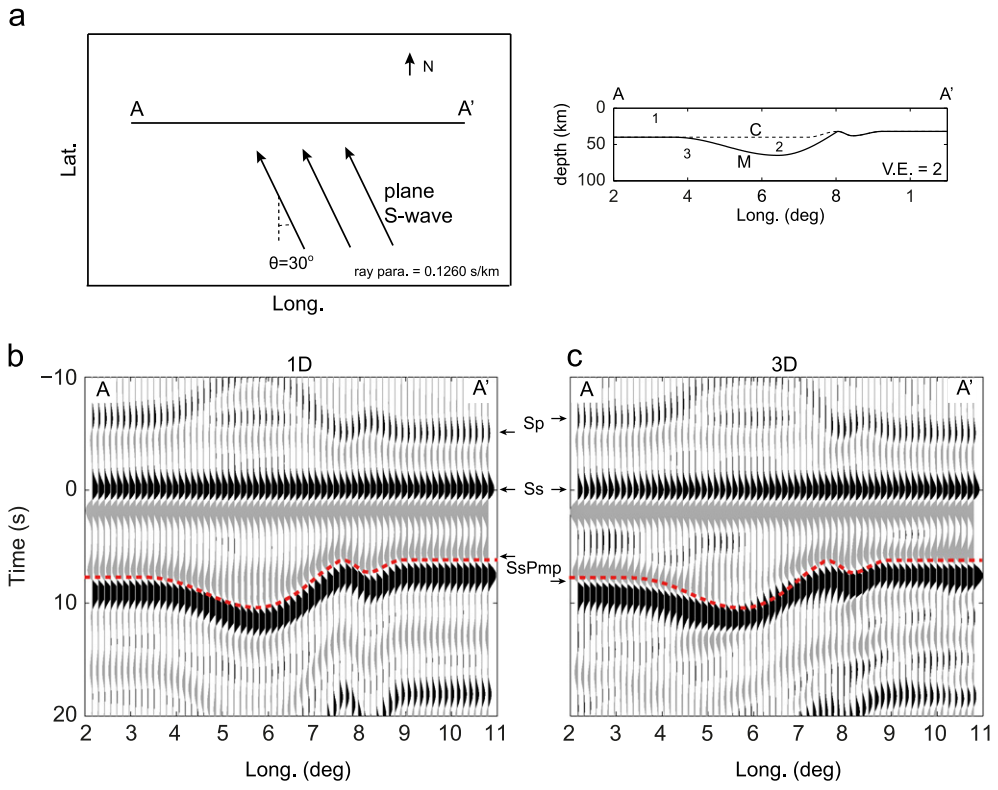

Fig. 6. Comparison of synthetic VDSS between 1-D and 3-D waveform modeling. Left panel of (a) is a map view of array location and plane wave incidence. Right panel of (a) shows a vertical profile along the seismic array AA'. "C" is the Conrad discontinuity and "M" is the Moho. *P*-wave speed is 6.3 km/s, 7.3 km/s and 8.1 km/s in region 1, 2 and 3, respectively. V_P/V_S ratio is kept constant at 1.8. (b) 1-D synthetic VDSS with main crustal phases marked on the right. (c) 3-D synthetic VDSS. Central frequency of the source wavelet is 4 s. Red curves mark the arrival-times of the *SsPmp* phase based on the 1-D model. (For interpretation of the references to color in this figure caption, the reader is referred to the web version of this article.)

models should be small, as the steepest dip of the Moho (near the eastern margin of the Ordos plateau) is only about $\sim 10^{\circ}$.

To quantify these effects, we calculated synthetic seismograms using a 3-D, finite difference algorithm (Virieux, 1986; Moczo et al., 2000). Since data are available only along a 2-D array, we used key features identified from Fig. 4d and assumed that properties of the lithosphere is constant in the direction normal to the array (Fig. 6a). Nevertheless, we take into account full 3-D effects of propagating teleseismic, plane-waves incident from a back-azimuth of 150°. For *S*-waves, the ray parameter is set to be 0.1260 s/km, the value for station JB15 near the middle of the profile (Table 1; Figs. 6a and 4d). For detailed information of the 3-D waveform modeling, see Supplementary material S4.

Fig. 6c and b compares synthetic seismograms for scattered *S*-wave field from 3-D wave propagation with those from 1-D models that are most sensitive to topside reflections off the Moho of the *SsPmp* phase. As expected, the two sets of synthetic seismograms are generally similar. The 3-D simulation accounts for wave-front healing away from scatters and the resulting profile is smoother than that from 1-D modeling. The latter tends to show artificial steps if the change in crustal thickness is significant among nearby stations. At any rate, the typical errors in crustal thickness are about 2–3 km ($\sim$0.5 s variation in $T_{SsPmp\text{-}Ss}$). We also carried out corresponding simulations for RFs and the results from 3-D and 1-D models are almost identical, a direct result of near-vertical ray-paths of *P*-to-*S* conversions.

We tested different values of ray parameters for the incident *S*-wave and *P*-wave, and the results are nearly identical expect for anticipated, minor changes in $T_{SsPmp\text{-}Ss}$ (Eq. (1)) and $T_{Ps\text{-}Pp}$ (Eq. (2)). In sum, except for the worst-case scenario, 1-D approximation generally leads to an error of no more than ± 3 km ($\pm 6\%$) in estimated crustal thickness.

4. Discussions

4.1. Conrad discontinuity and lateral variation in crustal properties

VDSS and RF provide evidence for two interfaces beneath the Ordos plateau, both associated with an increase in impedance with depth. Based on seismic imaging and the results of waveform modeling, we interpret the deeper interface as the Moho and the one within the crust as the Conrad discontinuity. Thus over a distance of about 700 km across the NCC (Fig. 4d), there are pronounced lateral variations in crustal properties, including (1) rapid changes in total thickness, (2) the presence versus the absence of the Conrad discontinuity, and (3) variations in sharpness of the two discontinuities.

A marked change in crustal thickness, by almost a factor of two, occurs over a lateral distance of only about 100 km beneath the Shan-Xi graben (Figs. 2 and 4d). To the west of this transition, an intra-crustal (Conrad) discontinuity appears at a depth of 40 km as the total crustal thickness approaches 60 km (near 111°E; Figs. 3 and 4d). Indeed, a 650-km-long, N–S trending combined profile of seismic reflection and refraction across the Ordos plateau and the Yinshan orogenic belt also suggests two seismic interfaces at $\sim$40 km and $\sim$60 km depths beneath the northeastern Ordos plateau (Teng et al., 2010).

The Conrad discontinuity identified here extends over a distance of about 300 km but seems absent west of $\sim$108°E, where the Moho shoals to less than 50 km deep (Figs. 3 and 4d). In other words, much of the Ordos plateau is underlain by a thick crust, including a lenticular lower crust, whereas the thickness of the upper crust remains more-or-less constant. Note that the observed variations in crustal structures here are along an E–W trending profile (Fig. 1). Some N–S variations within the Ordos plateau might also exist (Wei et al., 2012).

The sharpness of the Conrad discontinuity and the Moho also varies laterally. For instance, at station FY05, *Ps* and *Sp* phases are both emergent (Fig. 4b), indicating a gradual change from the crust to the mantle (Fig. 4c). If defined by the largest radial gradient of wave-speeds within the crust, the Conrad discontinuity can be traced as far as station FY05, just east of 111°E (Fig. 4c and d). If one defines the Moho in an analogous manner, then beneath station FY05 the Moho is at a depth of about 60 km, some 30 km deeper than the Conrad discontinuity.

We note that one can also view the change from crust to uppermost mantle as a gradual transition over a depth range of almost 30 km (Fig. 4c). A similar but more extreme situation occurs beneath central Tibet (Tseng et al., 2009; Nowack et al., 2010), where several strong interfaces, with impedance contrast as high as that of the Moho, were detected between 40 and 80 km depths. These findings are fundamentally incompatible with an oversimplified notion that the crustal–mantle transition is a single, sharp interface artificially defined as the Moho.

The sharpness of the Moho varies also under the Taihang Mountains (eastern end of Fig. 4d). Distinct *Ps* and *Sp* phases indicate a sharp Moho beneath station HD01 (Fig. 4), while a barely discernible *Ps* phase signifies a gradual transition beneath station HD08 (Fig. S7).

4.2. Crustal isostasy

Considering that the thermal age of its upper crust is Archean, viscous relaxation over billions of years is unlikely to have left the Ordos plateau far out of crustal isostasy. Airy isostasy, however, clearly fails here. In Fig. 4d, we compare the crustal thickness as constrained by seismic observations with that predicted by Airy isostasy (assuming an average crustal density of 2800 kg/m^3, a density increase of 450 kg/m^3 across the Moho, and a reference crustal thickness of 38 km at sea-level). Not surprisingly, since the variation in surface elevation is modest across much of this plateau (Fig. 3), the Airy model would not predict marked lateral variations in total crustal thickness. Based on our results, Airy isostasy under-predicts crustal thickness by 15–20 km in the region of thick crust (Fig. 4d).

The large crustal thickness under the Ordos block can be reconciled with gravity measurements through the presence of mafic lower crust below the Conrad discontinuity. Using an average thickness of $\sim$41 km and a density of $\sim$2800 kg/m^3 for the upper crust, crustal isostasy predicts a density of 3040 kg/m^3 for a lower crust of $\sim$17 km in thickness (Fig. 4c, Station JB15). The predicted density is typical of mafic rocks in regions of low geotherms, such as granulite and gabbro, before turning into eclogite/garnet pyroxenite (Christensen and Mooney, 1995). Such a prediction is consistent with a corresponding *P*-wave speed of about 7.4 km/s, about the same as estimated through waveform modeling (Fig. 4a–c). Our model also readily explains the observation of negligible free-air gravity anomaly over much of the Ordos plateau (Wei et al., 1981).

4.3. Implications for geodynamics

The current configuration of the lithosphere under the Ordos may be regarded as a proxy for the initial condition of the eastern NCC, where a cratonic keel no longer exists. In particular, we suggest that a lower crust of mafic granulite, which is still present under the Ordos, also existed under the eastern NCC where the prior presence of a dense lower crust was necessary (but not, by itself, sufficient) for foundering of the lower crust and underlying lithosphere. Following this hypothesis, the difference in stability

between eastern and western NCC then simply reflects whether the lower crust has transformed into eclogite or not.

The cause of eclogitization can be attributed to dehydration associated with subduction of the intervening oceanic lithosphere prior to the collision between northern and southern China terranes (e.g., Gao et al., 2004, 2008). It seems equally probable that subduction of the Paleo-Pacific plate during and before mid-Mesozoic may also have transported large quantities of water beneath eastern China to cause eclogitization of the lower crust there.

Another important constraint is the thickness of the lower crust. Eclogitized lower crust must be both denser than the upper mantle and sufficiently abundant for the lower crust to founder. We can obtain a rough estimate of the minimum spatial scale of a foundering eclogite body from Stokes' law. The terminal (maximum) speed of a spherical blob sinking through a viscous medium is (e.g., Lamb, 1994)

$$v_t = (4/3)\pi r^3(\Delta\rho)g/6\pi r\eta \quad (3)$$

where r is the radius of the sphere; $\Delta\rho$ the density contrast; g the gravitational acceleration; and η is the coefficient of viscosity. Note that v_t is proportional to the square of the size of the blob, r, whereas the relationship is linear in all other terms.

As a first approximation, v_t is of the order of 1 mm/yr (that is, 100 km/100 Ma), assuming that the foundering began in the Mesozoic and eclogitized lower crust sank through about 100 km of lithospheric mantle. Under upper mantle conditions, eclogite would be denser than the surrounding mantle by 200–400 kg/m^3 (Gao et al., 2004; Jordan, 1988; Rudnick and Fountain, 1995). For commonly accepted values of mantle viscosity, from 10^{20} to 10^{21} Pa s (e.g., Turcotte and Schubert, 2002), a $\Delta\rho$ of 300 kg/m^3 leads to a value of about 7 km for r, assuming the higher value for viscosity. Indeed, numerical simulations showed that high viscosity of the mantle keel seems to be necessary to maintain its longevity (e.g., Shapiro et al., 1999). So if the viscosity of the keel is higher by even another order of magnitude, then the characteristic length scale of the blob must be about 20 km to sustain the same terminal speed of sinking. These rough estimates are comparable to the thickness of mafic lower crust under the Ordos plateau, lending support to the proposition that the initial configuration of crust below the eastern NCC was similar to the current situation beneath the western NCC.

Since an active case of decratonization does not seem to exist, one cannot entirely dismiss the alternative that received little attention so far. The eastern NCC may have lost (or never fully developed) its deep keel earlier than the Mesozoic, before the production of the "adakite-like" magmatism.

5. Conclusions

Application of Virtual Deep Seismic Sounding (VDSS) and conventional receiver functions (RF) to data from a 1000 km-long, east–west trending profile reveals intriguing variations in crustal properties across the North China craton (NCC). Contrary to a modest crustal thickness of 45–50 km predicted by the Airy model and previous RF studies, the crust under the stable Ordos plateau (or the western NCC) appears to reach a thickness of over 60 km on its eastern flank. Under the central NCC, crustal thickness changes rapidly, by about a factor of two over a distance of only 100 km under the Shan-Xi graben. Beneath the Taihang Mountains, the crust shoals eastward to its eastern margin. Farther to the east, the crust remains thin and nearly flat-lying under most of the eastern NCC (Fig. 2).

The thick crust under the Ordos plateau is characterized by a distinct layer of lower crust, likely of mafic composition and reaching a maximum thickness of about 20 km. A clear boundary between the upper and the lower crust, interpreted as the Conrad discontinuity, can be traced over a distance of about 300 km. Overall crustal isostasy is maintained if the lower crust has a density close to 3000 kg/m^3, consistent with a mafic composition.

Using the current properties of the crust under the stable Ordos plateau as a proxy for the initial condition prior to reactivation of the eastern NCC, an important necessary condition for the hypothesis of lower crust foundering is satisfied: a substantial layer of mafic lower crust must exist, so subsequent transformed into eclogite/garnet pyroxenite can generate the excess negative buoyancy that is required to cause foundering.

In addition to providing new constraints on the structure and evolution of the lithosphere of the North China Craton, our results emphasize the importance of using more than a single technique to investigate properties of the lithosphere. In cases where the crust–mantle transition is complex or gradual, VDSS offers a physically averaged estimate of the crustal thickness which falls within the thick zone of transition (Fig. 4d; Tseng et al., 2009). Meanwhile, receiver functions help detect and characterize impedance contrasts within the crust.

Acknowledgements

We thank R. Rudnick, W. McDonough, S.-L. Chung, C.-T. Lee, L. Chen, Y.-C. Zheng, and X.-F. Shang for discussions and useful comments on the manuscript. We are indebted to all members of the seismology group at Peking University, whose industrious work in the field provided essential data for this study. Comments from the Editor (P. M. Shearer) and two anonymous reviewers help improve the quality of the manuscript. The data collected at this east-west PKU array were fully supported by the China NSF grant 90814002. Additional supports come from US NSF grants EAR99-09362 (Hi-CLIMB), 05-51995 and 06-35419 (W.-P. Chen), and a Shell graduate research fellowship (C.-Q Yu).

Appendix A. Supporting information

Supplementary data associated with this article can be found in the online version at 10.1016/j.epsl.2012.09.027.

References

562 Brigade (Ed.), 1979. Tectonic Framework and Seismicity Map of China (1:4 million, in Chinese). Chinese Academy of Geological Sciences, Beijing.
Ammon, C.J., 1991. The isolation of receiver effects from teleseismic P waveforms. Bull. Seismol. Soc. Am. 81, 2504–2510.
Chen, L., Cheng, C., Wei, Z.G., 2009. Seismic evidence for significant lateral variations in lithospheric thickness beneath the central and western North China Craton. Earth Planet. Sci. Lett. 286, 171–183.
Chen, L., Zheng, T., Xu, W., 2006. A thinned lithospheric image of the Tanlu Fault zone, eastern China: constructed from wave equation based receiver function migration. J. Geophys. Res. 111, B09312.
Chen, W.-P., Nabelek, J., 1988. Seismogenic strike-slip faulting and the development of the North China basin. Tectonics 7, 975–989.
Christensen, N., Mooney, W., 1995. Seismic velocity structure and composition of the continental crust: a global view. J. Geophys. Res. 100, 9761–9788.
Gao, S., Rudnick, R.L., Xu, W.L., Yuan, H.L., Liu, Y.S., Walker, R.J., Puchtel, I.S., Liu, X., Huang, H., Wang, X.R., 2008. Recycling deep cratonic lithosphere and generation of intraplate magmatism in the North China Craton. Earth Planet. Sci. Lett. 270, 41–53.
Gao, S., Rudnick, R.L., Yuan, H.L., Liu, X.M., Liu, Y.S., Xu, W.L., Ling, W.L., Ayers, J., Wang, X.C., Wang, Q.H., 2004. Recycling lower continental crust in the North China craton. Nature 432, 892–897.
Griffin, W., Zhang, A., O'Reilly, S., Ryan, C., 1998. Phanerozoic evolution of the lithosphere beneath the Sino-Korean craton. In: Flower, M.F.J., et al. (Eds.), Mantle Dynamics and Plate Interactions in East Asia. AGU, Washington, D. C, pp. 107–126.
Huang, Z., Li, H., Zheng, Y., Peng, Y., 2009. The lithosphere of North China Craton from surface wave tomography. Earth Planet. Sci. Lett. 288, 164–173.

Jia, S.X., Zhang, X.K., 2005. Crustal structure and comparison of different tectonic blocks in North China. Chin. J. Geophys. 48 (3), 611–620. (in Chinese).
Jordan, T.H., 1978. Composition and development of the continental tectosphere. Nature 274, 544–548.
Jordan, T.H., 1981. Continents as a chemical boundary layer. Philos. Trans. R. Soc. London A301, 359–373.
Jordan, T.H., 1988. Structure and formation of the continental tectosphere. J. Petrol., 11–37. (Special Lithosphere Issue).
Kusky, T., Windley, B., Zhai, M.G., 2007. Tectonic Evolution of the North China Block: From Orogen to Craton to Orogen, vol. 280. Geological Society, London, pp. 1–34 (Special Publications).
Lamb, H., 1994. Hydrodynamics. 6/e. Cambridge University Press 599.
Langston, C.A., 1979. Structure under Mount Rainier, Washington, inferred from teleseismic body waves. J. Geophys. Res. 84, 4749–4762.
Li, C., Van der Hilst, R.D., 2010. Structure of the upper mantle and transition zone beneath Southeast Asia from traveltime tomography. J. Geophys. Res. 115, B07308, http://dx.doi.org/10.1029/2009JB006882.
Li, S., Mooney, W., Fan, J., 2006. Crustal structure of mainland China from deep seismic sounding data. Tectonophysics 420, 239–252.
Liu, D.-Y., Nutman, A.P., Compston, W., Wu, J.S., Shen, Q.-H, 1992. Remnants of $>=3800$ Ma crust in the Chinese part of the Sino-Korean craton. Geology 20, 339–342.
Menzies, M., Xu, Y., Zhang, H., Fan, W., 2007. Integration of geology, geophysics and geochemistry: a key to understanding the North China Craton. Lithos 96, 1–21.
Menzies, M.A., Fan, W., Zhang, M., 1993. Palaeozoic and cenozoic lithoprobes and the loss of >120 km of Archaean lithosphere, Sino-Korean craton, vol. 76. China Geological Society, London, pp. 71–81 (Special Publications).
Moczo, P., Kristek, J., Halada, L., 2000. 3D fourth-order staggered-grid finite-difference schemes: stability and grid dispersion. Bull. Seismol. Soc. Am. 90 (3), 587–603.
Nowack, R.L., Chen, W.-P., Tseng, T.L., 2010. Application of Gaussian-beam migration to multiscale imaging of the lithosphere beneath the Hi-CLIMB array in Tibet. Bull. Seismol. Soc. Am. 100, 1743–1754.
Pearson, D., 1999. The age of continental roots. Dev. Geotectonics 24, 171–194.
Polet, J., Anderson, D.L., 1995. Depth extent of cratons as inferred from tomographic studies. Geology 23, 205–208.
Randall, G., 1989. Efficient calculation of differential seismograms for lithospheric receiver functions. Geophys. J. Int. 99, 469–481.
Rudnick, R.L., Fountain, D.M., 1995. Nature and composition of the continental crust: a lower crustal perspective. Rev. Geophys. 33, 267–309.
Shapiro, S.S., Hager, B.H., Jordan, T.H., 1999. Stability and dynamics of the continental tectosphere. Dev. Geotectonics 24, 115–133.
Teng, J.W., Wang, F.Y., Zhao, W.Z., Zhang, Y.Q., Zhang, X.K., Yan, Y.F., Zhao, J.R., Li, M., Yang, H., Zhang, H.S., Ruan, X.M., 2010. Velocity structure of layered block and deep dynamic process in the lithosphere beneath the Yinshan orogenic belt and Ordos Basin. Chin. J. Geophys. 53 (1), 67–85. (in Chinese).
Tian, X., Teng, J., Zhang, H., Zhang, Z., Zhang, Y., Yang, H., 2011. Structure of crust and upper mantle beneath the Ordos Block and the Yinshan Mountains revealed by receiver function analysis. Phys. Earth Planet. Inter. 184, 186–193.
Tseng, T.-L., Chen, W.-P., Nowack, R.L., 2009. Northward thinning of Tibetan crust revealed by virtual seismic profiles. Geophys. Res. Lett. 36, L24304, http://dx.doi.org/10.1029/2009GL040457.
Turcotte, D.L., Schubert, G., 2002. Geodynamics. 2/e. Cambridge University Press 238–242.
Virieux, J., 1986. P-SV wave propagation in heterogeneous media: velocity-stress finite-difference method. Geophysics 51 (4), 889–901.
Wei, M.H., Wang, Q.M., Shi, Z.H, Yin, X.H., Liu, Z.P., Zhang, Y.M, 1981. A preliminary study of the free air gravity field in China continent. Seismol. Geol. 3, 47–60. (in Chinese).
Wei, Z.G., Chen, L., Xu, W.W., 2012. Crustal thickness and Vp/Vs ratio of the central and western North China Craton and its tectonic implications. Geophys. J. Int. 186, 385–389.
Wilson, D., Aster, R., 2005. Seismic imaging of the crust and upper mantle using regularized joint receiver functions, frequency-wave number filtering, and multimode Kirchhoff migration. J. Geophys. Res. 110, B05305, http://dx.doi.org/10.1029/2004JB003430.
Wu, F.Y., Lin, J.Q., Wilde, S.A., Zhang, X.O., Yang, J.H., 2005. Nature and significance of the Early Cretaceous giant igneous event in eastern China. Earth Planet. Sci. Lett. 233, 103–119.
Xu, Y.G., 2001. Thermo-tectonic destruction of the Archaean lithospheric keel beneath the Sino-Korean Craton in China: evidence, timing and mechanism. Phys. Chem. Earth Part A 26, 747–757.
Yuan, Y., Hu, S., Wang, H., Sun, F., 2007. Meso-Cenozoic tectonothermal evolution of Ordos basin, central China: insights from newly acquired vitrinite reflectance data and a revision of existing paleothermal indicator data. J. Geodyn. 44, 33–46.
Zhao, G., Sun, M., Wilde, S.A., Sanzhong, L., 2005. Late Archean to Paleoproterozoic evolution of the North China Craton: key issues revisited. Precambrian Res. 136, 177–202.
Zhao, L., Allen, R.M., Zheng, T., Hung, S.H., 2009. Reactivation of an Archean craton: constraints from P-and S-wave tomography in North China. Geophys. Res. Lett. 36, L17306, http://dx.doi.org/10.1029/2009GL039781.
Zheng, T.Y., Zhu, R.X., Zhao, L., Ai, Y.S., 2012. Intralithospheric mantle structures recorded continental subduction. J. Geophys. Res. 117, B03308, http://dx.doi.org/10.1029/2011JB008873.